Weather and Climate Extremes 35 (2022) 100408

Contents lists available at ScienceDirect

Weather and Climate Extremes

journal homepage: www.elsevier.com/locate/wace

Future change in extreme precipitation in East Asian spring and Mei-yu seasons in two high-resolution AGCMs

Chao-An Chen [a,*], Huang-Hsiung Hsu [a], Hsin-Chien Liang [a], Ping-Gin Chiu [b], Chia-Ying Tu [a]

[a] Research Center for Environmental Changes, Academia Sinica, Taiwan
[b] Geophysical Institute, University of Bergen, Bergen, Norway

ARTICLE INFO

Keywords:
Extreme precipitation
High-resolution AGCM
Large ensemble simulation
Mei-yu
Spring
East Asia

ABSTRACT

Precipitation in the spring and Mei-yu seasons, the main planting and growing period in East Asia, is crucial to water resource management. Changes in spring and Mei-yu extreme precipitation under global warming are evaluated based on two sets of high-resolution simulations with various warming pattern of sea surface temperature (SST'$_{spa}$). In the spring season, extreme precipitation exhibits larger enhancements over the northern flank of the present-day prevailing rainy region and a tendency of increased occurrence and enhanced intensity in the probability distribution. These changes imply a northward extension of future spring rainband. Although the mean precipitation shows minor change, enhanced precipitation intensity, less total rainfall occurrence, and prolonged consecutive dry days suggest a more challenging water resource management in the warmer climate. The projected enhancement in precipitation intensity is robust compared with the internal variability related to initial conditions ($\hat{\sigma}_{int}$) and the uncertainty caused by SST'$_{spa}$ ($\hat{\sigma}_{\Delta SST}$). In the Mei-yu season, extreme precipitation strengthens and becomes more frequent over the present-day prevailing rainband region. The thermodynamic component of moisture flux predominantly contributes to the changes in the spring season. In the Mei-yu season, both the thermodynamic and dynamic components of moisture flux enhance the moisture transport and intensify the extreme precipitation from southern China to northeast Asia. Compared with spring season, projecting future Mei-yu precipitation is more challenging because of its higher uncertainty associated with 1) the $\hat{\sigma}_{int}$ and $\hat{\sigma}_{\Delta SST}$ embedded in the projections and 2) the model characteristics of present-day climatology that determines the spatial distribution of precipitation enhancement.

1. Introduction

Precipitation in the East Asian monsoon, an important part of the Asian monsoon system, is characterized by a marked seasonal cycle consisting of one main wet period in summer and one dry period in winter. Two transition periods, namely spring and fall, occur between the wet and dry periods (Chou et al., 2009; Chen et al., 2019). The wet season is further divided into two subseasons, namely the Mei-yu and typhoon seasons (Hsu et al., 1999; Wang and Lin, 2002; Hung and Hsu 2008; Chou et al., 2009; Chen et al., 2019). After a relatively dry period in fall and winter, precipitation in spring and Mei-yu, which are the main planting and growing seasons in East Asia, is a major factor affecting water resource management, agriculture policy, disaster prevention, and other socioeconomic impacts. Changes in precipitation, particularly those caused by extreme events such as drought and heavy rainfall are expected to exert substantial impacts on East Asia in the warmer climate.

The Coupled Model Intercomparison Project (CMIP) phase 5 (CMIP5; Taylor et al., 2012) models projected an increase in precipitation in summer with medium confidence accompanied by an enhanced daily rainfall intensity, greater heavy precipitation amount, and the prolonged dry spell in East Asia under global warming scenario (Christensen and Coauthors, 2013). More monsoonal rainfall and heavier extreme precipitation events are newly confirmed (e.g., Chen et al., 2020; Ha et al., 2020) from the CMIP phase 6 (CMIP6; Eyring et al., 2016) model simulations. However, in respect of extreme precipitation changes in spring and Mei-yu seasons in the warmer future, a more comprehensive assessment that considers model limitation and embedded uncertainties are relatively unexplored.

The horizontal resolution in coupled general circulation models are often insufficiently high to realistically simulate the precipitation intensity and seasonal march during Mei-yu (e.g., Kusunoki and Arakawa

* Corresponding author.
E-mail address: joanne22@gate.sinica.edu.tw (C.-A. Chen).

https://doi.org/10.1016/j.wace.2022.100408
Received 2 July 2021; Received in revised form 26 November 2021; Accepted 17 January 2022
Available online 19 January 2022
2212-0947/© 2022 The Authors. Published by Elsevier B.V. This is an open access article under the CC BY-NC-ND license (http://creativecommons.org/licenses/by-nc-nd/4.0/).

2015; Endo and Kitoh 2016; Kusunoki 2016; Chen et al., 2019), likely resulting in low confidence in the future projections of extreme precipitation (Endo and Kitoh 2016). While the simulation of seasonal northward migration of precipitation has been improved in CMIP6 model, more efforts for realistic simulations in extreme events and rainfall occurrence are still needed (Chen et al., 2021), particularly in spring and fall seasons. High-resolution global atmospheric models driven by prescribed sea surface temperature fluctuations have been proven to simulate more reliable extreme precipitation and widely used in projecting future changes in extreme precipitation (e.g., Kitoh and Kusunoki 2008; Endo et al., 2012; Mizuta et al., 2012). However, systematic biases in the spatial distribution of sea surface temperature (SST) remain in many state-of-the-art general circulation models in present-day simulations (e.g., Flato and Coauthors, 2013; Lin 2007; Li and Xie 2014). In addition, the spatial variability of changes in SST (SST'_{spa}) among models is a key source of uncertainty in regional projections in global warming simulations (Christensen and Coauthors, 2013; Huang et al., 2013; Ma and Xie 2013; Chadwick et al., 2014). With improvements in the physics and resolution of climate models in recent decades, quantification of the uncertainty in future climate projections has gradually been emphasized.

Uncertainties associated with various emission scenarios and climate model formulations have been a major focus in CMIP experiments (Meehl et al., 2000, 2007; Taylor et al., 2012; Eyring et al., 2016). On the other hand, more and more attention has also been paid to the uncertainties arising from internal variability through large ensemble simulations (hereafter LES; Deser et al., 2014; Kay et al., 2015). Particularly, the LES provides a large sample size of rarely-occurring extreme events, which have much larger uncertainty, and enables the evaluation of the distribution and probability of extreme event changes from a statistical perspective. The LES approach has been proven to yield more comprehensive information and higher confidence in assessment (Xie et al., 2015; Kitoh and Endo 2019). Considering narrowing the uncertainty in extreme precipitation projections, high horizontal resolution atmospheric general circulation model (AGCM) LES forced by various SST'_{spa} can be useful for exploring the potential future changes.

Simulations conducted using the Meteorological Research Institute (MRI)-AGCM with different SST'_{spa} demonstrated an intensification of Mei-yu precipitation (Kusunoki and Mizuta 2008; Kusunoki et al., 2011), extreme precipitation (Endo et al., 2012), and moisture flux convergence (e.g., Kusunoki et al., 2011). To pursue further following this approach, in this study we conduct a series of experiments using the high-resolution atmospheric model (HiRAM) developed at the Geophysical Fluid Dynamics Laboratory and compare the HiRAM results with a high-resolution AGCM LES named "Database for Policy Decision Making for Future Climate Change" (d4 PDF; Mizuta et al. 2017) to estimate changes in extreme precipitation and uncertainty in East Asia during the spring and Mei-yu seasons in the warmer climate. These different warming experiments benefit us to identify whether the projected extreme precipitation changes are robust in response to overall warming or variably depending on ensemble sizes, SST'_{spa}, or models. Section 2 describes our models, experimental setup, and methodology. Section 3 estimates the changes in spatial distribution and probability distribution of extreme precipitation indices, the related uncertainty, and mechanisms associated with precipitation change in future projections. Conclusions and discussion are provided in section 4.

2. Models, experiments, and methods

2.1. HiRAM

HiRAM was developed based on AM2 (Anderson and Coauthors, 2004; Zhao et al., 2009). Finer resolutions and physics-based modifications associated with the convection scheme enabled HiRAM to simulate more realistic features of precipitation, particularly in East Asia. Freychet et al. (2017) demonstrated that HiRAM performed well in simulating seasonal extreme indices in East Asia in the present-day climate simulation. Chen et al. (2019) reported that HiRAM simulated not only the general structure but also the seasonal evolution of precipitation in East Asia with a score higher than those obtained using most AGCMs and coupled atmosphere–ocean general circulation models (AOGCMs) at coarser resolution. The good skill yields higher confidence in using HiRAM for the projections in warmer climate.

In this study, we use HiRAM to conduct a series of time-slice experiments that are driven by the prescribed SST in present-day and future warmer climate simulations. The horizontal resolution is about 50 km per horizontal atmospheric grid. In present-day simulations, designated as the control experiment, HiRAM is forced by the observed SST obtained from HadISST1 (Rayner et al., 2003) and the historical greenhouse gas concentration (Donner et al., 2011) during 1984–2008, hereafter denoted as HIS_Ctrl. In global warming simulations, the greenhouse gas concentration following the Representative Concentration Pathways 8.5 (RCP8.5) scenario (Meinshausen et al., 2011) together with SST'_{spa} are used as forcing to drive HiRAM. The four sets of SST'_{spa} are as follows: an ensemble-averaged SST change of 28 CMIP5 models (Mizuta et al., 2014; denoted as RCP_Ens) and three SST change patterns (denoted as RCP_C1, RCP_C2, and RCP_C3) by 2075–2099. The three SST change patterns are derived by performing cluster analysis of SST changes that were projected by the 28 CMIP5 models (Mizuta et al., 2014). The observed interannual variation in SST during 1984–2008 is added to SST changes as lower-boundary forcing. Using the same observed SST interannual variation in both present-day and future experiments allows us to evaluate how the current precipitation with the same interannual variability of SST might change under the forcing of anthropogenic greenhouse effect and a warmer ocean. These four experiments represent the effect of the spatial structure of SST changes. A comparison between four sets of experiments enables us to discuss the responses of regional precipitation to various SST'_{spa} in the warmer climate, i.e., uncertainty arising from different SST change patterns. Each experiment consists of four simulation members with different initial conditions to represent the uncertainty associated with the model internal variability. See Chen et al. (2019) and Fig. 2 herein for more details of the experiments.

2.2. d4PDF

The d4PDF data set comprises model outputs by forcing the MRI-AGCM3.2 (MRI-AGCM, version 3.2; with a horizontal resolution of 60 km; Mizuta et al., 2012) with projected SST changes from six CMIP5 AOGCMs. The model formulation is identical to that of MRI-AGCM3.2H, which is reported to be more efficient in simulating the seasonal evolution of East Asian precipitation (No. 16 in Fig. 1c in Chen et al., 2019) compared with most AGCMs and AOGCMs.

In this study, historical and +4K future climate simulations in d4PDF are investigated as present-day and future warming scenarios, respectively. The historical (1951–2010) experiment forced by observed COBE-SST2 SST(Centennial Observation-Based Estimates of SST, version 2; Hirahara et al., 2014) and greenhouse gases, consists of 100-member simulations with different atmospheric initial conditions and small SST perturbations (δSSTs) in the historical data set. Global warming experiments are conducted by forcing the model with the projected SST in the condition of +4K warming in the global mean surface air temperature relative to that in the historical experiment. The +4K warming is equivalent to the condition approximately the 2090s under the RCP8.5 scenario, a period equivalent to that in HiRAM projection. The six long-term averaged SST warming patterns projected by CCSM4, GFDL_CM3, HadGEM2-AO, MIROC5, MPI-ESM-MR, and MRI_CGCM3 (denoted as CC, GF, HI, MI, MP, and MR, respectively; Mizuta, 2017) are selected and added to the observational SST after removing the long-term trend. The six CMIP5 models are selected to represent the range of the uncertainty among all CMIP5 models. For each SST'_{spa} experiment, the warming pattern was normalized by a

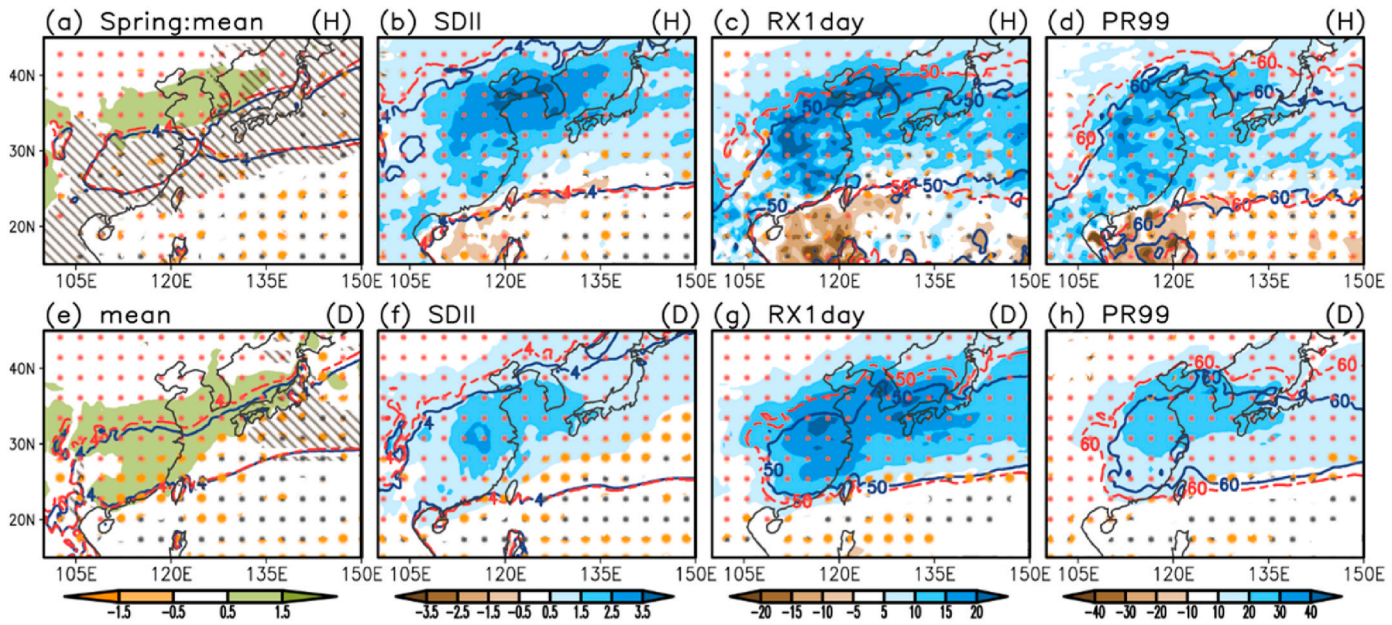

Fig. 1. Ensemble average of precipitation changes (shaded colors) in (a) seasonal mean, (b) SDII, (c) RX1day, and (d) PR99, estimated from the ensemble average of four SST'_{spa} in HiRAM, and (e)–(h) the ensemble average of six SST'_{spa} in d4PDF in the spring season. Red (orange) dots mark the region where more than 3/4 (1/2) of SST'_{spa} experiments exhibit the statistically significant tendency consistent with the ensemble change. The 10% significance level using the Wilcoxon–Mann–Whitney test is adopted here. The blue-solid (red-dashed) contour represents climatology in the historical (warming) experiment. The hatched shading denotes regions with decreased rainfall frequency. (For interpretation of the references to color in this figure legend, the reader is referred to the Web version of this article.)

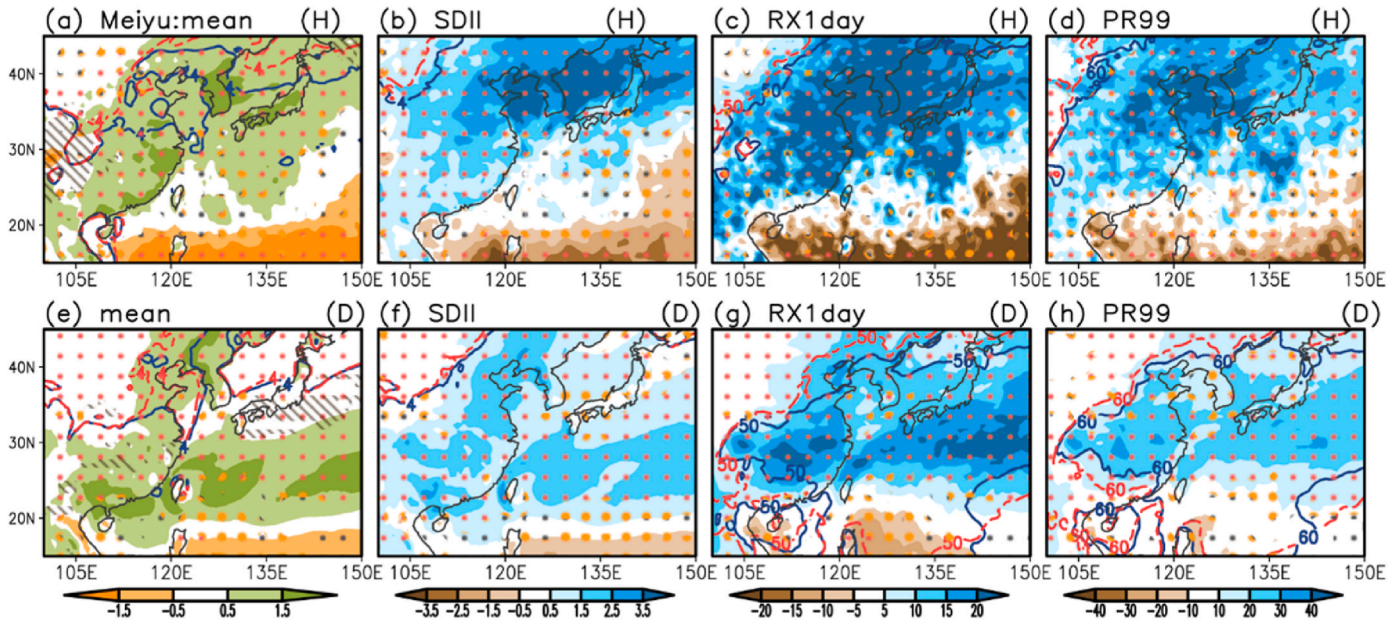

Fig. 2. Same as Fig. 1, but for (a–d) HiRAM and (e–f) d4PDF in the Mei-Yu season.

scaling factor to reflect +4K warming in the global mean surface air temperature. 15-member ensemble simulations are conducted using each model, yielding a total of 90 members in the future warming data set. See Mizuta (2017) for the completed description of the experiment. We note that the SST'_{spa} used in experiments between HiRAM and d4PDF are different. The impact of the uncertainty across SST'_{spa} in HiRAM and d4PDF is stated in the uncertainty estimation.

2.3. Definition of rainy season and extreme indices

In this study, the period during 10th–27th pentad (i.e., February 15–May 15) and the 28th–41st pentad (i.e., May 16–July 24) are selected as the spring and Mei-yu seasons, respectively, following the definitions in Chou et al. (2009) and Chen et al. (2019). Indices for extreme precipitation are estimated based on the definition provided by the Expert Team on Climate Change Detection and Indices (ETCCDI) (Sillmann et al., 2013; Duan et al., 2015). We investigate the simple daily intensity (SDII), maximum 1-day precipitation (RX1day), maximum 5-day precipitation (RX5day), extreme precipitation intensity (PR99), consecutive dry days (CDD), and total rainfall occurrence (Table 1) in the spring and Mei-yu seasons. In both HiRAM and d4PDF, we examine 25-year daily data during 1984–2008 in the historical

Table 1
Definition of precipitation and temperature extreme indices. The threshold for wet day is 0.1 mmday^{-1} in this study.

Index	Index Name	Definition	Unit
SDII	Simple daily intensity	Annual total precipitation divided by the number of wet days	mmday^{-1}
RX1day	Maximum 1-day precipitation	Annual maximum of 1-day precipitation amount	mm
RX5day	Maximum 5-day precipitation	Annual maximum of 5-day precipitation amount	mm
PR99	Extreme precipitation intensity	The 99th percentile of the precipitation intensity on wet days during the analyzed period.	mm
TotFq	Total rainfall occurrence	Annual number of wet days (daily precipitation ≥0.1 mm)	days
CDD	Consecutive dry days	Annual maximum number of consecutive dry days (daily precipitation <0.1 mm)	days

simulation and 2075–2099 in the warming scenario simulation. Changes in seasonal extreme precipitation under global warming are estimated by subtracting the results of the historical simulation from those of warming scenario experiments, and the statistical significance of these changes are evaluated by Wilcoxon-Mann-Whitney test (Chu, 2002; Wilks, 2011). The ensemble average of extreme precipitation change from four (six) SST′$_{spa}$ experiments in HiRAM (d4PDF) is presented.

Fig. S1 presents the performance of HiRAM and d4PDF in simulating extreme precipitation indices against those in the Tropical Rainfall Measuring Mission (TRMM; Huffman et al., 2007 and 2010) during 1999–2008. Results of 18 AGCMs from CMIP5 are also compared. Both HiRAM and d4PDF have a higher score in all indices than most of AGCMs. HiRAM gains lower scores in SDII than d4PDF but higher score in all other heavy rainfall indices (i.e., RX1day, RX5day, and PR99). All AGCMs obtain a lower skill score for PR99 than those for other indices. Scores are higher for most indices in the spring season than in the Mei-yu season, indicating that more efforts are needed to improve the simulation of the extreme rainfall event during the Mei-yu season in which the rainfall tends to be much more of convective type and therefore more extreme. Generally, HiRAM and d4PDF perform better than most of the AGCMs in the AMIP group (Fig. S1), and also gain higher skill scores than the AMIP ensemble in all indices. Same evaluation based on GPCC (Global Precipitation Climatology Centre; Ziese et al., 2020) but for model performance over East Asian land region is also considered (Fig. S2). The results generally display similar distribution to those examined based on TRMM. These results suggest that high-resolution models, such as HiRAM and MRIAGCM3.2, yield higher confidence in the assessment of future precipitation changes.

2.4. Estimation of uncertainties in future climate projections

In addition to the anthropogenic warming effect, the projected changes are also affected by different initial conditions (one type of internal variability) and SST spatial patterns, resulting in the uncertainty in projected changes. It is important to evaluate the signal-to-noise ratio (or uncertainty) before identifying change signals. For example, detected changes should be larger than the variability (here identified as the standard deviation) induced by different initial conditions and SST′$_{spa}$. To evaluate the total variance and its decomposed components associated with internal variability and SST′$_{spa}$, we adopt a statistical method based on an analysis of variance concept (Sugi et al., 1997; Endo et al., 2017). The variance of the internal variability ($\widehat{\sigma}^2_{int}$) describes the deviation in each simulation from the ensemble mean of different initial conditions and SST perturbations (δSSTs) (Eq. (1)),

$$\widehat{\sigma}^2_{\text{int}} = \frac{1}{N(n-1)} \sum_{i=1}^{N} \sum_{j=1}^{n} \left(\chi_{ij} - \overline{\chi}_i\right)^2 \tag{1}$$

where N is the number of different SST′$_{spa}$ (i.e., $N = 4$ for HiRAM and $N = 6$ for d4PDF) and n is the number of members with different atmospheric initial conditions and δSSTs (i.e., $n = 4$ for HiRAM and $n = 15$ for d4PDF). Thus, χ_{ij} represents the future change in the given index for the i-th SST′$_{spa}$, the j-th member of different initial condition and δSST, and $\overline{\chi}_i$ represents the ensemble average of the i-th SST′$_{spa}$. ˆ denotes the best estimator of a population quantity.

The variance associated with different SST warming patterns ($\widehat{\sigma}^2_{\Delta SST}$) is considered by the deviation in the ensemble mean of each SST′$_{spa}$ experiment from that of all experiments but excluding the variance associated with internal variability (Eqs. (2) and (3)). $\overline{\overline{\chi}}$ represents the mean of all simulations.

$$\widehat{\sigma}^2_{\text{EM\_δSST}} = \frac{1}{N-1} \sum_{i=1}^{N} \left(\overline{\chi}_i - \overline{\overline{\chi}}\right)^2 \tag{2}$$

$$\widehat{\sigma}^2_{\Delta\text{SST}} = \widehat{\sigma}^2_{\text{EM\_δSST}} - \frac{1}{n}\widehat{\sigma}^2_{\text{int}} \tag{3}$$

Therefore, the total variance ($\widehat{\sigma}^2_{tot}$) is obtained as follows:

$$\widehat{\sigma}^2_{tot} = \widehat{\sigma}^2_{\Delta\text{SST}} + \widehat{\sigma}^2_{\text{int}} \tag{4}$$

3. Results

3.1. Spatial distribution of changes in extreme indices

3.1.1. Spring season

Fig. 1 shows the mean precipitation in spring in the historical and warming scenarios overlaid with corresponding changes due to global warming. The colored dots represent the consistency (i.e., the numbers of SST′$_{spa}$ experiments) between the ensemble average and SST′$_{spa}$ experiments. Only the grid points with statistically significant change are counted. In HiRAM His_Ctrl, the ensemble-averaged spring rainband (blue solid contour in Fig. 1a) resembling the observation (not shown) extends northeastward from southeastern China to southern Japan. The margin of 4 mmday^{-1} for mean precipitation slightly expands northward in the ensemble of RCP experiments (red dash contour in Fig. 1a), and increased precipitation (marked in green shading) is identified over the north flank of the spring rainband around northern China and the Korean Peninsula. By contrast, decreased precipitation (mostly between −0.5 and 0 mmday^{-1}) occupies the southern half of the rainband area (not shown). The boundaries of SDII (4 mmday^{-1}), RX1day (50 mm), and PR99 (60 mm) demonstrate a more northward expansion in precipitation strength and extremes. Significant enhancements in SDII, RX1day, and PR99 are found in almost the entire region between 20°N and 40°N in the majority of SST′$_{spa}$ experiments (red dots), with larger enhancements over northern China, the Korean Peninsula, and Japan. Weakened SDII, RX1day, PR99, and RX5day (Fig. S2c) are found around Taiwan, the South China Sea (SCS), and northern Luzon island. However, the mean precipitation change is small over these regions. It is worth noticing that SDII, RX1day, and PR99 exhibit a significant increase over southeastern China, although changes in mean precipitation are small. In terms of changes in rainfall frequency, a decreased total rainfall occurrence (brown hatched; see also Fig. S2a) generally overlaps with the climatological mean spring rainband where the precipitation intensity is enhanced. From southern China to northeast Asia, the HiRAM results demonstrate a tendency toward heavier and more frequent extreme events.

Similar features of precipitation change as shown above are also found in d4PDF. The northward expansion of the northern flank of the climatological mean precipitation, in conjunction with a larger enhancement (Fig. 1e–h) in the SDII, RX1day, PR99, and RX5day (Fig. S2), is consistently found in all six SST warming patterns in d4PDF simulations (red dots). However, the change in the precipitation frequency is more complicated. From six various SST warming experiments

in d4PDF, the decreased precipitation frequency is consistently found only around the western North Pacific (WNP) region east of Japan (hatched in Fig. 1e) comparing to the wide spread decrease projected by HiRAM (hatched in Fig. 1a, see also Fig. S2d).

3.1.2. *Mei-yu season*

In the Mei-yu season, the mean precipitation (Fig. 2a) increases along the climatological rainband from southern China to the Korean Peninsula and Japan accompanied by enhanced SDII, RX1day, PR99, and RX5day (Fig. 2b–d and Fig. S3, respectively) in more than 3/4 of SST'_{spa} experiments (marked by red dots) in HiRAM. An increased mean precipitation (Fig. 2e) accompanied by enhanced SDII, RX1day, PR99, and RX5day (Fig. 2f–h and Fig. S3, respectively) is also observed in d4PDF but in the area extending eastward from southern China to the northern Philippine Sea. The area that exhibited enhanced precipitation in d4PDF is located to the south of that in HiRAM.

3.2. *Uncertainties in future climate projection*

To evaluate the uncertainty in projected precipitation changes shown in Figs. 1 and 2, we compute the total variance ($\widehat{\sigma}^2_{tot}$) from all experiments and the relative contributions from internal variability ($\widehat{\sigma}^2_{int}$) and SST'_{spa} ($\widehat{\sigma}^2_{\Delta SST}$) based on the definition in section 2.4. The squared roots of the above variabilities are presented for comparison with precipitation changes. For the evaluation, we selected southern China (23°N–33°N, 105°E–120°E, hereafter SC) and northeast Asia (30°N–40°N, 125°E–140°E, hereafter NEA) as two representatives of prevailing rainy regions in observation. These regions are the prevailing rainband regions where the observational mean precipitation at each grid point is higher than 4 $mmday^{-1}$, and the variance of precipitation is higher than one standard variation. Although northern China (33°N–43°N,110°E–120°E, hereafter NC) is not in the prevailing rainband region in the present-day climate, it is also considered because of the marked future enhancement of extreme precipitation in both HiRAM and d4PDF.

In spring, for both SC and NEA in HiRAM and d4PDF (Fig. 3a–d), the values of all precipitation indices except the mean precipitation are higher in the ensemble change term (Prec′; blue bars in Fig.3) than in the total spread among all members ($\widehat{\sigma}_{tot}$), which is dominated by the internal variability associated with various initial conditions ($\widehat{\sigma}_{int}$). The value of the ensemble change is almost twice that of $\widehat{\sigma}_{tot}$ in all indices in both models except the smaller values of RX1day and RX5day in SC in HiRAM (Fig. 3a). Compared with the uncertainty (i.e., the orange, gray and yellow bars), the higher values of projected changes (blue bars) observed in both models suggest that the enhanced SDII, RX1day, RX5day, and PR99 in projections can be attributed mostly to the RCP8.5 warming scenario. Whereas the prescribed SST'_{spa} in HiRAM and d4PDF are different, the smaller $\widehat{\sigma}_{\Delta SST}$ indicates less impact of SST'_{spa} on the enhancement of extreme indices over the East Asia land region.

During the Mei-yu season, similar results are also found in SC in both HiRAM and d4PDF (Fig. 3e–f). The ensemble change in each precipitation index except RX5day in d4PDF is larger than $\widehat{\sigma}_{tot}$ in all simulations, indicating the robustness of enhanced extreme indices although with smaller contrast compared with the results in the spring season. The variance contributed from $\widehat{\sigma}_{int}$ is still considerably larger than that from $\widehat{\sigma}_{\Delta SST}$. In the NEA region, the enhanced mean precipitation and extreme precipitation intensity are robust in HiRAM (Fig. 3g). By contrast, in d4PDF (Fig. 3h), $\widehat{\sigma}_{tot}$ is almost as large as the ensemble change for the SDII and even larger than ensemble changes for mean precipitation and

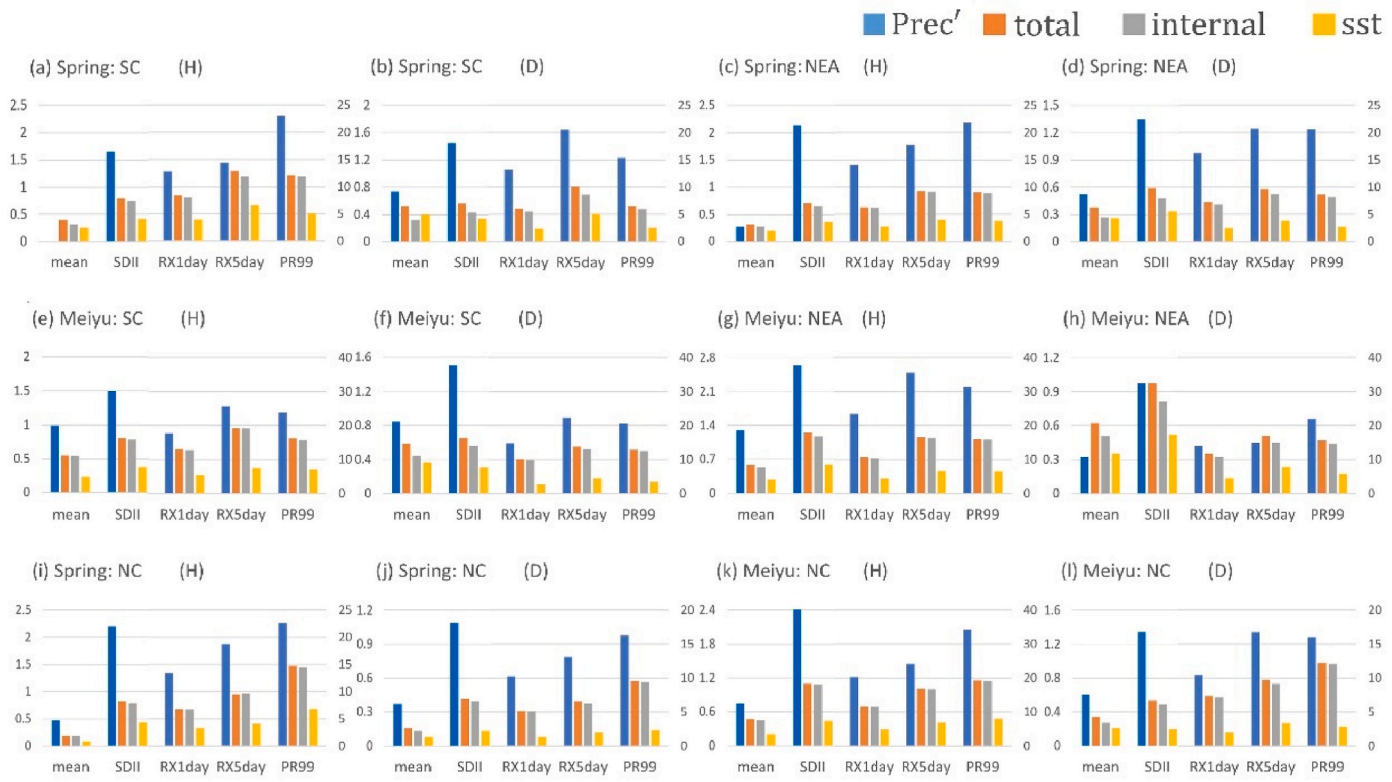

Fig. 3. Regional estimation for ensemble changes in seasonal mean precipitation and four indices (Prec′; blue bars) against the total spread among all members ($\widehat{\sigma}_{tot}$; orange bars) and the spread associated with both internal variability ($\widehat{\sigma}_{int}$; gray bars) and SST'_{spa} ($\widehat{\sigma}_{\Delta SST}$; yellow bars) in HiRAM (abbreviated as H) and d4PDF (abbreviated as D) for the spring and Mei-Yu seasons. The scale on the left (unit: $mmday^{-1}$) is for the mean and SDII, and the scale on the right (unit: mm) is for RX1day, RX5day, and PR99. SC denotes southern China (23°N–33°N, 105°E–120°E), NEA denotes northeast Asia (30°N–40°N, 125°E–140°E), and NC denotes northern China (33°N-43°N, 110°E–120°E). (For interpretation of the references to color in this figure legend, the reader is referred to the Web version of this article.)

RX5day. The ensemble change in PR99 remains considerably larger than uncertainties arising from various initial conditions and SST'_{spa} forcing patterns. Fig. 3g–h reveals the discrepancy between models, implying uncertainty in future precipitation changes in the NEA region.

Changes in NC are much more significant than those in SC and NEA. As shown in Fig. 3i–l, the values of ensemble changes in all indices are almost double those in $\widehat{\sigma}_{tot}$ and $\widehat{\sigma}_{int}$. The variability from SST'_{spa} is particularly small in this region. The robustness of the enhanced mean precipitation and extreme rainfall intensity implies the larger warming impacts on extreme rainfall in the NC region, where less precipitation is observed in the present-day climate. The $\widehat{\sigma}_{\Delta SST}$ impact in both HiRAM and d4PDF remain minor in the SC, NEA, and NC regions.

By contrast, the projection over the oceanic region is considerably different. As shown in Figs. S4a–4b, in the WNP region (20°N–30°N, 125°E–140°E) $\widehat{\sigma}_{int}$ and $\widehat{\sigma}_{\Delta SST}$ of all indices are considerably higher than ensemble changes in the spring season, indicating a large uncertainty in the projected rainfall in the WNP region. In the Mei-yu season, in most of the extreme indices, $\widehat{\sigma}_{int}$ is the dominant uncertainty source embedded in the enhanced extreme precipitation (Figs. S4c–4d).

3.3. Probability distribution of extreme precipitation

We investigate the probability distribution of changes in precipitation indices. For a specific latitudinal belt (e.g., 25°–30°N, 110°E–140°E in Fig. S5), the distribution of extreme indices exhibits a future shift toward a wet-get-wetter and dry-get-dryer condition, indicating a more frequent occurrence of both stronger rainfall events and longer dry spells during the spring and Mei-yu seasons in every SST'_{spa} experiment in HiRAM and d4PDF. The differences between present-day and future warming experiments is even larger in the higher latitudes (e.g., 35°N–40°N; Fig. S6). A similar shift toward stronger precipitation is found in other latitudes. The probability distribution averaged over 110°E–140°E for every latitudinal grid between 20°N and 45°N is shown in Fig. 4, in which blue-solid and red-dashed contours mark the number of occurrences exceeding 150 in historical and warming experiments, respectively. In the spring season, the occurrence of SDII 2–4 $mmday^{-1}$ (Fig. 4a) is the most frequently observed in the present-day experiment at 20°N–25°N; the most recurrent SDII enhances to 8–12 $mmday^{-1}$ over 30°N–35°N and gradually weakens northward to 45°N. The red-dashed contour representing the future distribution evidently shifts toward stronger precipitation in the north of 25°N. In Fig. 4a–c and 4e-4g, the red versus blue contours indicate that heavier SDII, RX1day, and PR99 events more frequently occur in warmer climate simulations by both HiRAM and d4PDF. A consistent shift toward stronger precipitation is also found in RX5day (Fig. S7). The shift is more evident in the maroon-green shaded region that indicates the tendency of less light and more heavy precipitation events in the warmer climate. Such changes are robust signals in different SST'_{spa} experiments (red dots). The shifting contour and the shading color are more distinct at the north of 30°N (i.e., the north of the peak frequency in the control experiment), corresponding to the northward expansion of the spring rainband shown in Fig. 1. Regarding the dry spell index, to the south of 35°N, longer-duration CDD events occur more frequently (maroon color) and shorter-duration CDD events occur less frequently (green) in both HiRAM and d4PDF. However, compared with other indices, the orange dots shown in Fig. 4d and h suggest that the CDD has less consistent changes between different SST'_{spa} experiments, especially north of 35°N. Moreover, less consistency in CDD changes are found between HiRAM and d4PDF. The uncertainty between the simulations is also compared with the above changes (Fig. S8). The orange dots in Fig. S8 indicate that changes in extreme indices are considerably larger than $\widehat{\sigma}_{tot}$ in the simulations. Generally, colored dots indicate consistency between simulations in terms of the shift in the probability distribution. However, changes in CDD display a larger uncertainty, especially in d4PDF.

In the Mei-yu season, similar shifts are identified. However, the distinct shift (as reflected by contours and shadings) occur near the peak frequency in the present-day climate, implying the enhancement of the precipitation intensity over the present-day rainband region. The inconsistent distribution in maximum changes between HiRAM and d4PDF reflects the inconsistency in the spatial pattern shown in Fig. 2. Changes in CDD are less consistent between two models and more uncertain among SST'_{spa} experiments (Fig. 4l and p). The uncertainty associated with the total variance in the Mei-yu season is also estimated (Fig. S8). The colored dots reflect considerable distinction between the changes and $\widehat{\sigma}_{tot}$. Compared with results obtained in the spring season, broader areas marked by gray dots are observed in the Mei-yu season, implying a larger uncertainty in projections in the Mei-yu season.

3.4. Mechanisms for changes in extreme precipitation

To understand the factors of large-scale environment accounting for the changes in extreme indices during spring and Mei-yu seasons in HiRAM and d4PDF, we diagnose the low-level moisture transport ($MT = Vq$) at 850 hPa, where V is horizontal wind (u and v), and q is specific humidity.

3.4.1. Spring season

In the current climate, the spring season exhibits a larger MT (light blue vector in Fig. 5a and c) from southern China to east Japan. In the warming simulations in both HiRAM and d4PDF, the ensemble average of the change in moisture transport (MT', deep blue vector in Fig. 5a and c) displays a transport enhancement generally exceeding 35% (more than 100% in certain areas; green shading indicating the ratio of change in $[(uq)^2 + (vq)^2]^{0.5}$) agreeing with the spatial distribution of enhanced extreme indices (Fig. 1). The enhanced MT' is consistently identified in every SST warming pattern in HiRAM (Figs. S9a–S9d) and d4PDF (Figs. S10a–S10f). The thermodynamic component of MT' associated with increased water vapor (MT'_{th}, i.e., $\overline{V}q'$; pink vector in Fig. 5b and d) is driven by the prevailing southwesterly in the current climate, transporting more moisture from the tropical to the extratropical region. Moreover, because the Pacific subtropical high extends westward and expands poleward (not shown) in the warmer climate, the dynamic component of MT' driven by anomalous circulation (MT'_{dy}, i.e., $V'\overline{q}$; green vector in Fig. 5b and d) generally weakens MT'_{th}, but is relatively weak compared with MT'_{th}. For the individual SST'_{spa} experiment, MT'_{th} shows similar distribution while MT'_{dy} displays a larger spread, particularly in the oceanic region (Figs. S9e–S9h and Fig. S10g-S10l). Generally, these findings indicate that the thermodynamic component predominantly contributes to the enhancement of MT furnishing the intensification of extreme precipitation from southern China to east Japan.

3.4.2. Mei-yu season

The prevailing MT (light blue vector in Fig. 6a and c) associated with monsoon trough in the present-day climate flows from the SCS to northeast Asia. Under global warming, the ensemble average of MT' (deep blue vector in Fig. 6a and c) reveals a more than 35% enhancement from southern China to northeast Asia (green shaded region) corresponding to the regions with greater amplitude of increased extreme precipitation in Mei-yu season (Fig. 2), despite the regional inconsistency between HiRAM and d4PDF. Similar features can be identified in every SST'_{spa} experiment (Figs. S11a–11d and Figs. S12a–12f). Under global warming, MT'_{th} (pink vector in Fig. 6b and d) transports more moisture from the SCS into East Asia. In addition, the anomalous anticyclonic circulation around Taiwan and the Philippines is project to result in MT'_{dy} (green vector in Fig. 6b and d) that contributes to the enhanced MT from east China to northeast Asia. Features

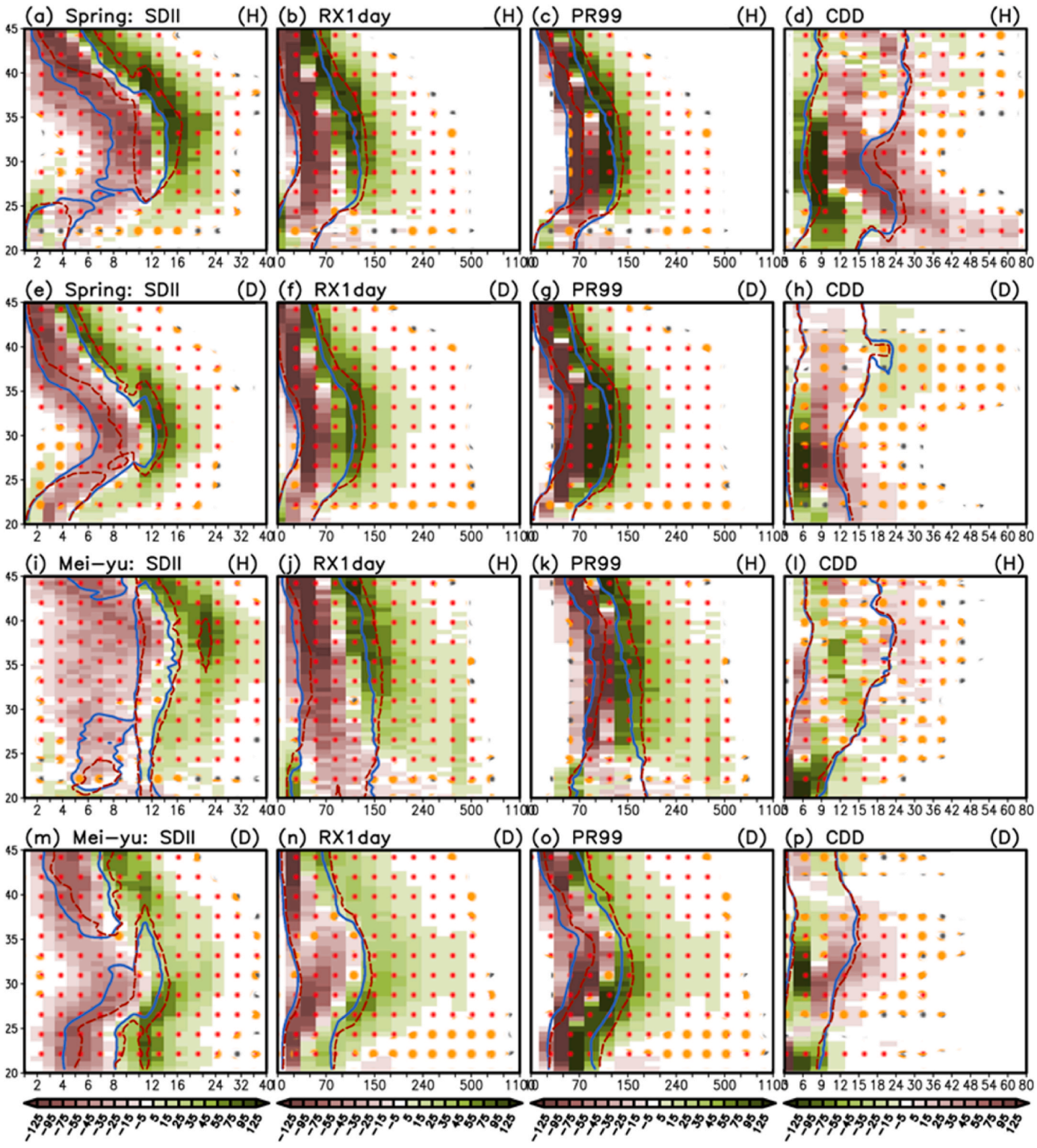

Fig. 4. Ensemble average of changes in the probability distribution (unit: frequency for 25-year period) estimated between 110°E–140°E along 20°N–45°N (y-axis) for (a) SDII, (b) RX1day, (c) PR99, and (d) CDD in HiRAM, and (e–h) in d4PDF in the spring season at 110°E–140°E. Same as (a–h), but for (i–p) the Mei-Yu season. Unit in the x-axis is that of each index (Table 1). Red (orange) dots mark the region where more than 3/4 (1/2) of SST'_{spa} experiments indicate the statistically significant tendency consistent with the ensemble average. The 10% significance level using the Chi-square test is adopted here. The blue-solid (red-dashed) contour represents the number of occurrences exceeding 150 in the historical (warming) experiment. (For interpretation of the references to color in this figure legend, the reader is referred to the Web version of this article.)

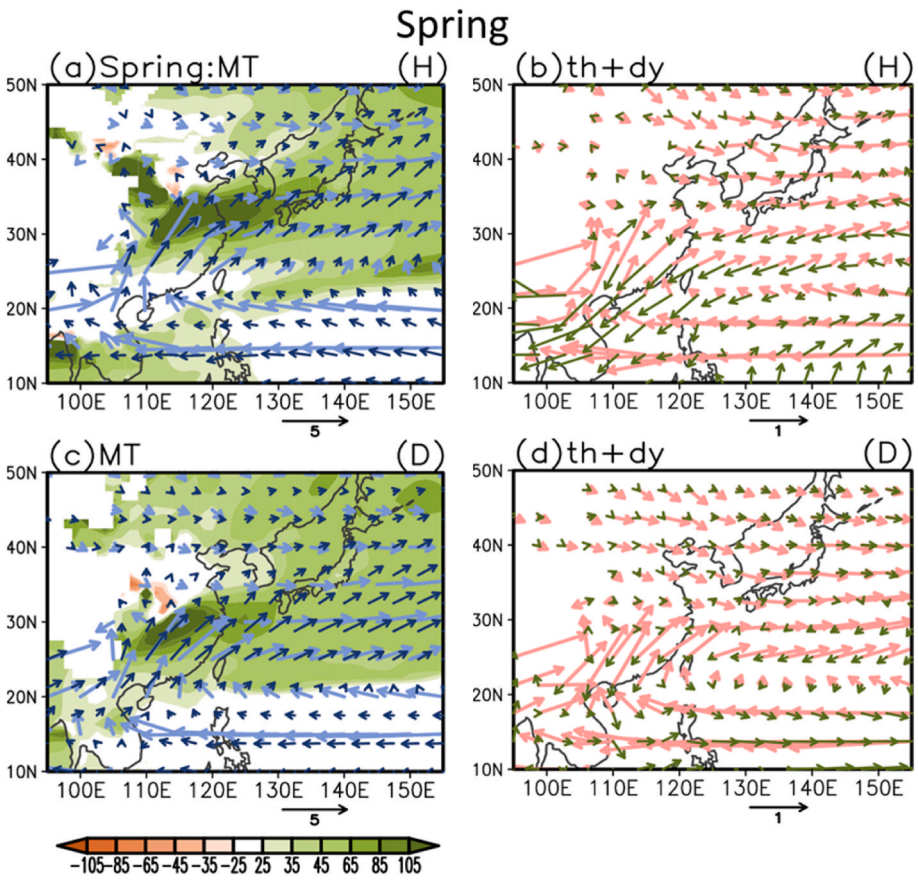

Fig. 5. Ensemble average of (a) changes in moisture transport (MT'; deep blue vector) and (b) the thermodynamic (pink vector) and dynamic (green vector) components of MT' in HiRAM in the spring season. The light blue vector represents the seasonal mean of moisture transport in the present-day climate simulation. The green shaded region denotes the ratio of increased MT (unit: %). (c–d) Same as (a–b) but for the results of d4PDF. (For interpretation of the references to color in this figure legend, the reader is referred to the Web version of this article.)

of MT'_{th} and MT'_{dy} described above are generally identifiable in each SST'_{spa} experiment (Figs. S11e–11h and S12g-12l). The global warming response of the monsoon trough and the ridge of the Pacific subtropical high could be a key factor accounting for MT'_{dy} in the Mei-yu season. Under the influence of global warming, the monsoon trough over the SCS weakens and retreats westward to the east of the Indochina Peninsula (the contrast of blue-red contours in Fig. 7a and c) whereas the Pacific subtropical high ridge extends westward into the SCS (positive shaded color in Fig. 7a and c). As a result, the low-level circulation over SCS reveals an anomalous anticyclonic circulation and a negative anomaly of relative vorticity in conjunction with a shrinking area with positive relative vorticity (contrast of blue-red contours in Fig. 7b and d).

Both MT'_{th} and MT'_{dy} benefit the enhancement of extreme indices from east China to northeast Asia in the Mei-yu season. While the contribution of MT'_{th} to MT' is similarly shown in HiRAM and d4PDF, a marked difference in MT'_{dy} is observed between HiRAM and d4PDF. The stronger positive contribution of MT'_{dy} in HiRAM is likely associated with the strongly enhanced subtropical high characterized by a westward-extended ridge over the SCS and the Philippine Sea (Fig. 7a). The enhanced anticyclone is also evident in d4PDF but mostly in lower latitudes between 15°N and 25°N (Fig. 7c). The details of low-level circulation change in every SST'_{spa} experiment are shown in Figs. S13 and S14.

3.4.3. *Mechanism accounting for the uncertainty in Mei-yu season*

The enhanced extreme indices projected by HiRAM occur mostly to the north of 30°N, whereas those projected by d4PDF occur mostly further south between 20°N and 40°N. The inconsistency in the location of the maximum enhancement of extreme indices indicates the higher uncertainty of future projection for the Mei-yu season. The location showing stronger enhancement of extreme indices appears to be related to the location of the weakened monsoon trough and enhanced subtropical high, particularly the westward-extended ridge (Fig. 7a and c), which are related to their present-day climatology in each model. Compared with d4PDF, HiRAM simulates a deeper monsoon trough in the present-day climate (blue solid contour in Fig. 7a), and a weakened monsoon trough (red dashed contour) appears as an anticyclonic anomaly in the warmer climate (positive color shading). The subtropical high shows the strongest enhancement (Fig. 7a) over the SCS and the Philippine Sea where the present-day monsoon trough resides; therefore, the southwesterly flow (the dark blue vectors and green vectors in Fig. 6a and b) in conjunction with significantly enhanced extreme precipitation are pushed more northward in HiRAM experiments. By contrast, the subtropical high is generally less enhanced and located relatively southward (Fig. 7c) in d4PDF; thus, the southwesterly flow enhances between 20°N and 40°N resulting in significantly enhanced extreme precipitation in the region south of that in HiRAM. These contrasting results suggest that both models projected an increase in the precipitation intensity associated with the Mei-yu frontal system; however, the exact location depends on the present-day climatology in each model. These responses are hypothesized to be dependent of model climatology. That is, model responses are proportional to the spatial distribution and strength of the WNP monsoon. Accordingly, HiRAM would yield a larger-scale and stronger anticyclonic change because of its stronger and larger-scale monsoon trough/anticyclone system (i.e., the WNP monsoon) in the present-day climatology (or model climatology). By contrast, the anticyclonic change in d4PDF would exhibit a weaker strength and a smaller spatial scale because of the inherently weaker and smaller-scale WNP monsoon in the model. An independent study is being planned to test this hypothesis.

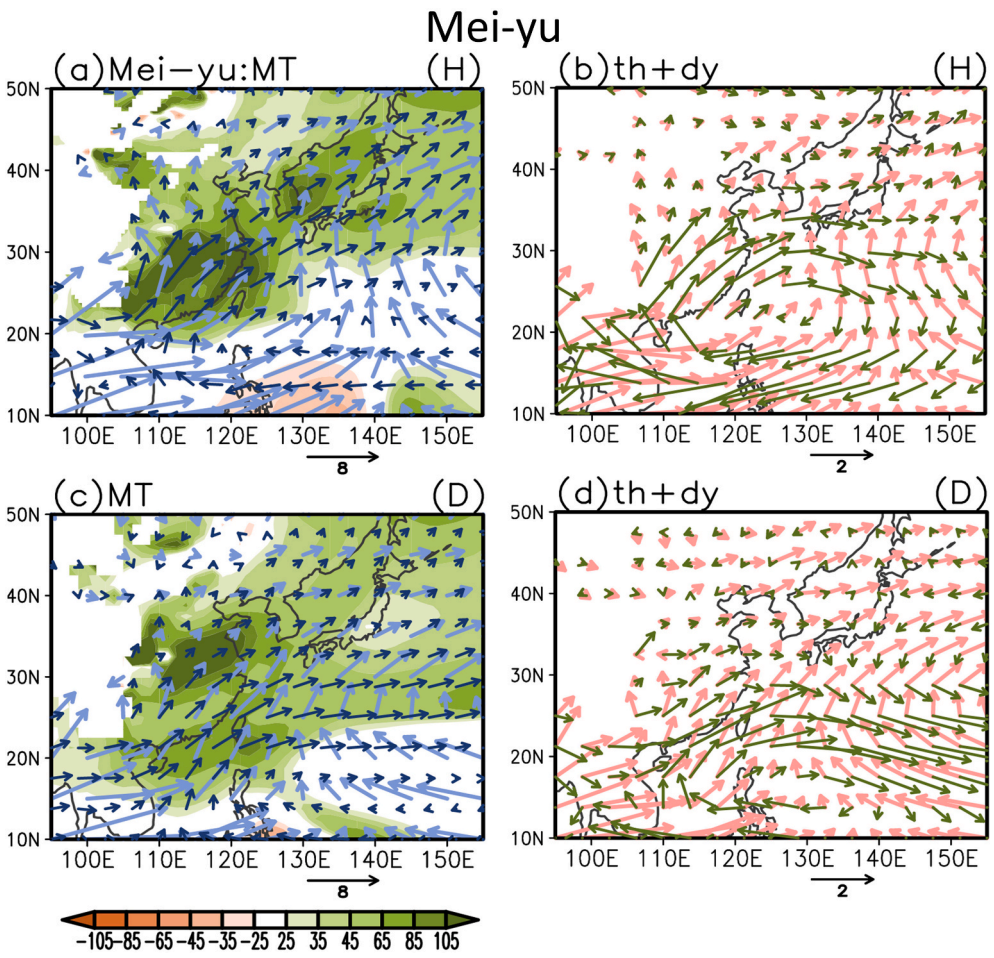

Fig. 6. Same as Fig. 5 but for the results in (a–b) HiRAM and (c–d) d4PDF in the Mei-yu season.

4. Conclusion and discussion

In the WNP-EA region, spring and Mei-yu seasons are two natural seasons occurring between the dry season during the WNP-EA winter monsoon and the mature phase of the summer monsoon. These two seasons are planting and growing seasons. Thus, changes in precipitation during these two seasons, particularly extreme events, are impactful in terms of flooding and drought in the region. In this study, we explore future changes projected in a series of high-resolution AGCM simulations using HiRAM and d4PDF. Although AGCM simulations using HiRAM and d4PDF do not consider the air–sea interaction, the findings in the Mei-yu season are consistent with the tendency projected by CMIP models (Christensen and Coauthors, 2013; Chiang et al., 2019). In addition, these high-resolution data sets are composed of multiple-member simulations initiated from various initial conditions and forced by different SST warming patterns. These data sets enable us to evaluate both the changes in extreme precipitation during spring and Mei-yu seasons and the uncertainty associated with various SST warming patterns and internal variability arising from different initial conditions. Another benefit of using high-resolution AGCMs is their ability in resolving extreme precipitation. High-resolution AOGCMs are still rare for climate simulations and projections, thus limiting their applicability in an in-depth analysis as presented here. Data produced by the High-Resolution model intercomparison (HiResMIP) of CMIP6 are recently made available. A study like the current one but using the HiResMIP data is being conducted for a comparison with the findings reported here.

During the spring season, an increased mean precipitation is found along the northern flank of the climatological rainband, implying a northward extension of the rainy region. The rainfall intensity (SDII) and extreme precipitation indices are enhanced with an increase in mean precipitation. The precipitation intensity is generally enhanced between 20°N and 45°N, whereas the rainfall occurrence is declined in conjunction with prolonged CDD, leading to only a minor change in mean precipitation. Consistently, the changes in the probability distribution of extreme precipitation indices display a northward shift with more frequent extreme rainfall events, explaining the increase in mean precipitation in spring. It is worth noting that the most enhanced extreme cases in simulations are found mostly over the region with less precipitation in the present-day climate. CDD with a longer spell becomes more frequent in the southern part of the East Asian region (Fig. 4), suggesting that water resource management becomes more difficult in a warmer climate. The robustness of the aforementioned changes is also confirmed by comparing them with the decomposed variance from the SST-forced component and model internal variability, particularly in northern China, where is a region with less precipitation in the current climate.

Unlike the northward extension in spring, the mean precipitation in the Mei-yu season depicts the largest increase over the major rainy region in the present-day climate, consistent with previous studies (Kusunoki and Mizuta 2008; Kusunoki et al., 2011; Endo et al., 2012). The increased mean precipitation can be attributed to enhanced extreme precipitation, which also tends to occur more frequently at the end of the 21st century. These changes are robust over southern and northern China in both HiRAM and d4PDF. Over the northeast Asian region, enhanced extreme precipitation is robust in HiRAM but uncertain in d4PDF. This inconsistency between HiRAM and d4PDF implies a higher uncertainty in the future projection of extreme precipitation during the

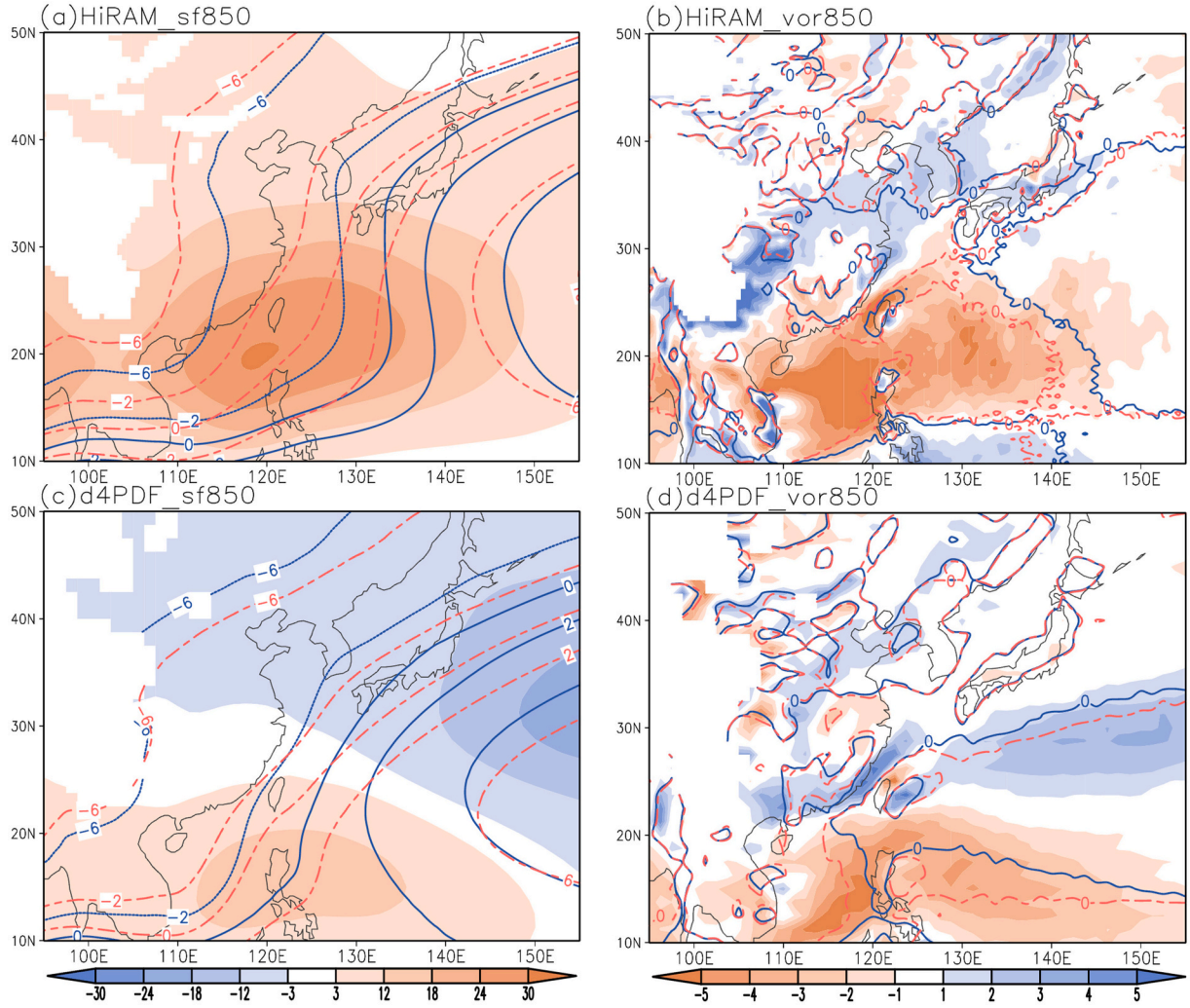

Fig. 7. Ensemble average of (a) stream function and (b) relative vorticity at 850 hPa in HiRAM in the Mei-yu season. Blue-solid and red-dashed contours are the seasonal mean in historical climate and warmer climate respectively (unit: (a) 1×10^6 m^2s^{-1} and (b) 1×10^{-5} s^{-1}). Shaded colors denote the changes under global warming (unit: (a) 1×10^5 m^2s^{-1} and (b) 1×10^{-6} s^{-1}). (c–d) Same as (a–b) but for the results in d4PDF simulations. (For interpretation of the references to color in this figure legend, the reader is referred to the Web version of this article.)

Mei-yu season than in the spring season.

This study examines changes in extreme precipitation in the East Asian region in global warming simulations by using two high-resolution AGCMs. We note that the SST'_{spa} conducted in experiments between HiRAM and d4PDF are different. Compared with the change in extreme indices, the uncertainties across SST'_{spa} in HiRAM and d4PDF are relatively small, implying the enhanced extreme intensities explored in this study are less affected by different SST'_{spa} except the WNP region in the spring season. In addition, although HiRAM has less simulation members than d4PDF does, most of the features during the spring season are similar between these models. The enhancement of extreme precipitation is associated with the enhanced moisture transport, which is dominated by the thermodynamic contribution in the spring season. In the Mei-yu season, thermodynamic and dynamic components both contribute to the enhanced moisture transport. The inconsistency in projected extreme indices in Mei-yu season between HiRAM and d4PDF is hypothesized to depend on the model mean state. HiRAM simulates a stronger and meridionally broader monsoon trough in Mei-yu season, thus projecting a stronger change that spreads further northward to eastern China. By contrast, MRI-AGCM3.2 used in d4PDF projects a weaker change over southern China and the Philippine Sea where the simulated present-day monsoon trough prevails. We noted that HiRAM and d4PDF are conducted by different observational SST, and the influence of different SST sources on simulated climatology is insignificant (not shown).

The study of dynamic and thermodynamic contributions provides a preliminary understanding that the change in the Pacific subtropical high is a key to the changes in precipitation. This is consistent with the recent findings in Park et al. (2020) and Wang et al. (2019) that linked intensified East Asian summer monsoon lifecycle and increased occurrence of extreme events to the variation of subtropical high in the WNP. However, in the future projection, some degrees of uncertainty of the monsoon trough/subtropical high system exist (Li et al., 2012; Shaw and Voigt 2015; He et al., 2017), and this uncertainty is seasonally dependent (Song et al., 2018). The CMIP5 future projection demonstrates an intensified subtropical high after the correction based on observational constraints using SST pattern (Chen et al., 2020). Future studies evaluating the high sensitivity of the circulation system to perturbations and various forcings can provide valuable information to narrow down the uncertainty in projecting extreme precipitation changes in the WNP-EA region.

CRediT authorship contribution statement

Chao-An Chen: Conceptualization, Methodology, Formal analysis, Investigation, Writing – original draft, Visualization, Funding

acquisition. **Huang-Hsiung Hsu:** Writing – review & editing, Supervision, Project administration, Funding acquisition. **Hsin-Chien Liang:** Data curation. **Ping-Gin Chiu:** Software. **Chia-Ying Tu:** Software.

Declaration of competing interest

The authors declare that they have no known competing financial interests or personal relationships that could have appeared to influence the work reported in this paper.

Acknowledgments

We thank two anonymous reviewers whose comments improved this paper. We thank the Program for Climate Model Diagnosis and Intercomparison (PCMDI) and the WCRP's Working Group on Coupled Modelling (WGCM) for collecting and archiving the AMIP-type simulations of WCRP CMIP5 multimodel data sets for analysis. We thank the climate modeling groups (listed in Table 1) for producing and making available their model outputs. All model data sets are available at https://esgf-node.llnl.gov/projects/cmip5/. We also thank the Meteorological Research Institute for providing the Database for Policy Decision Making for Future Climate Change (d4PDF) simulated from MRI_AGCM3.2. The d4PDF data sets are available at http://www.miroc-gcm.jp/~pub/d4PDF/index_en.html. The HiRAM simulations were conducted at the National Center for High-performance Computing, Taiwan. The HiRAM simulations are available at http://cclics.rcec.sinica.edu.tw/index.php/databases/data.html. This work was supported by Academia Sinica and the Ministry of Science and Technology (MOST) of Taiwan under MOST 108-2119-M-001-014-, MOST 109-2123-M-001-004-, MOST 110-2111-M-001 -002 -MY3, and MOST 110-2123-M-001-003-.

Appendix A. Supplementary data

Supplementary data to this article can be found online at https://doi.org/10.1016/j.wace.2022.100408.

References

Anderson, J.L., Coauthors, 2004. The new GFDL global atmosphere and land model AM2–LM2: evaluation with prescribed SST simulations. J. Clim. 17, 4641–4673. https://doi.org/10.1175/JCLI-3223.1.

Chadwick, R., Good, P., Andrews, T., Martin, G., 2014. Surface warming patterns drive tropical rainfall pattern responses to CO2 forcing on all timescales. Geophys. Res. Lett. 41 (2), 610–615.

Chen, C.A., Hsu, H.H., Hong, C.C., Chiu, P.G., Tu, C.Y., Lin, S.J., Kitoh, A., 2019. Seasonal precipitation change in the western North Pacific and East Asia under global warming in two high-resolution AGCMs. Clim. Dynam. 53 (9–10), 5583–5605.

Chen, Z., Zhou, T., Zhang, L., Chen, X., Zhang, W., Jiang, J., 2020. Global land monsoon precipitation changes in CMIP6 projections. Geophys. Res. Lett. 47 (14), e2019GL086902.

Chen, C.A., Hsu, H.H., Liang, H.C., 2021. Evaluation and comparison of CMIP6 and CMIP5 model performance in simulating the seasonal extreme precipitation in the western North Pacific and east Asia. Weather Clim. Extreme. 31, 100303 https://doi.org/10.1016/j.wace.2021.100303.

Chen, X., Zhou, T., Wu, P., 2020. Emergent constraints on future projections of the western North Pacific subtropical high. Nat. Commun. 11, 2802. https://doi.org/10.1038/s41467-020-16631-9.

Chiang, J.C., Fischer, J., Kong, W., Herman, M.J., 2019. Intensification of the pre-Meiyu rainband in the late 21st century. Geophys. Res. Lett. 46 (13), 7536–7545.

Chou, C., Huang, L.-F., Tseng, L., Tu, J.Y., Tan, P.H., 2009. Annual cycle of rainfall in the western North Pacific and east Asian sector. J. Clim. 22 (8), 2073–2094.

Christensen, J.H., Coauthors, 2013. In: Stocker, T.F., Qin, D., Plattner, G.-K., Tignor, M., Allen, S.K., Boschung, J., Nauels, A., Xia, Y., Bex, V., Midgley, P.M. (Eds.), Climate Phenomena and Their Relevance for Future Regional Climate Change, Climate Change 2013: the Physical Science Basis. Working Group I Contribution to the Fifth Assessment Report of the Intergovernmental Panel on Climate Change. Cambridge University Press, Cambridge, United Kingdom and New York, NY, USA., pp. 1217–1308

Chu, Pao-Shin, 2002. Large-scale circulation features associated with decadal variations of tropical cyclone activity over the central North Pacific. J. Clim. 15 (18), 2678–2689. https://doi.org/10.1175/1520-0442(2002)015%3C2678:LSCFAW%3E2.0.CO;2.

Deser, C., Phillips, A.S., Alexander, M.A., Smoliak, B.V., 2014. Projecting North American climate over the next 50 years: uncertainty due to internal variability. J. Clim. 27 (6), 2271–2296.

Duan, W., He, B., Takara, K., Luo, P., Hu, M., Alias, N.E., Nover, D., 2015. Changes of precipitation amounts and extremes over Japan between 1901 and 2012 and their connection to climate indices. Clim. Dynam. 45 (7), 2273–2292.

Donner, L.J., Wyman, B.L., Hemler, R.S., Horowitz, L.W., Ming, Y., Zhao, M., et al., 2011. The dynamical core, physical parameterizations, and basic simulation characteristics of the atmospheric component AM3 of the GFDL global coupled model CM3. J. Clim. 24 (13), 3484–3519.

Endo, H., Kitoh, A., Ose, T., Mizuta, R., Kusunoki, S., 2012. Future changes and uncertainties in Asian precipitation simulated by multiphysics and multi–sea surface temperature ensemble experiments with high-resolution Meteorological Research Institute atmospheric general circulation models (MRI-AGCMs). J. Geophys. Res. Atmos. 117 (D16) https://doi.org/10.1029/2012jd017874.

Endo, H., Kitoh, A., 2016. Projecting changes of the Asian summer monsoon through the twenty-first century. In: The Monsoons and Climate Change. Springer, Cham, pp. 47–66.

Endo, H., Kitoh, A., Mizuta, R., Ishii, M., 2017. Future changes in precipitation extremes in East Asia and their uncertainty based on large ensemble simulations with a high-resolution AGCM. Solanus 13, 7–12.

Eyring, V., Bony, S., Meehl, G.A., Senior, C.A., Stevens, B., Stouffer, R.J., Taylor, K.E., 2016. Overview of the coupled model intercomparison project phase 6 (CMIP6) experimental design and organization. Geosci. Model Dev. (GMD) 9 (5), 1937–1958.

Flato, G., Coauthors, 2013. Evaluation of climate models. In: Stocker, T.F., Qin, D., Plattner, G.-K., Tignor, M., Allen, S.K., Boschung, J., Nauels, A., Xia, Y., Bex, V., Midgley, P.M. (Eds.), Climate Change 2013: the Physical Science Basis. Contribution of Working Group I to the Fifth Assessment Report of the Intergovernmental Panel on Climate Change. Cambridge University Press, Cambridge, United Kingdom and New York, NY, USA.

Freychet, N., Duchez, A., Wu, C.H., Chen, C.A., Hsu, H.H., et al., 2017. Variability of hydrological extreme events in East Asia and their dynamical control: a comparison between observations and two high-resolution global climate models. Clim. Dynam. 48 (3–4), 745–766.

Ha, K.J., Moon, S., Timmermann, A., Kim, D., 2020. Future changes of summer monsoon characteristics and evaporative demand over Asia in CMIP6 simulations. Geophys. Res. Lett. 47 (8), e2020GL087492.

He, C., Wu, B., Zou, L., Zhou, T., 2017. Responses of the summertime subtropical anticyclones to global warming. J. Clim. 30 (16), 6465–6479.

Hirahara, S., Ishii, M., Fukuda, Y., 2014. Centennial-scale sea surface temperature analysis and its uncertainty. J. Clim. 27 (1), 57–75.

Hsu, H.H., Terng, C.T., Chen, C.T., 1999. Evolution of large-scale circulation and heating during the first transition of Asian summer monsoon. J. Clim. 12 (3), 793–810.

Huffman, G.J., Adler, R.F., Bolvin, D.T., Gu, G., Nelkin, E.J., Bowman, K.P., Hong, Y., Stocker, E.F., Wolff, D.B., 2007. The TRMM multi-satellite precipitation analysis: quasi-global, multi-year, combined-sensor precipitation estimates at fine scale. J. Hydrometeorol. 8, 38–55.

Huffman, G.J., et al., 2010. The TRMM multi-satellite precipitation analysis (TMPA). In: Hossain, F., Gebremichael, M. (Eds.), Chapter 1 in Satellite Rainfall Applications for Surface Hydrology. Springer Verlag, ISBN 978-90-481-2914-0, pp. 3–22.

Huang, P., Xie, S.P., Hu, K., Huang, G., Huang, R., 2013. Patterns of the seasonal response of tropical rainfall to global warming. Nat. Geosci. 6 (5), 357–361.

Hung, C.W., Hsu, H.H., 2008. The first transition of the Asian summer monsoon, intraseasonal oscillation, and Taiwan mei-yu. J. Clim. 21 (7), 1552–1568.

Kay, J.E., Deser, C., Phillips, A., Mai, A., Hannay, C., Strand, G., et al., 2015. The Community Earth System Model (CESM) large ensemble project: a community resource for studying climate change in the presence of internal climate variability. Bull. Am. Meteorol. Soc. 96 (8), 1333–1349.

Kitoh, A., Kusunoki, S., 2008. East Asian summer monsoon simulation by a 20 km mesh AGCM. Clim. Dynam. 31, 389–401. https://doi.org/10.1007/s00382-007-0285-2.

Kitoh, A., Endo, H., 2019. Future changes in precipitation extremes associated with tropical cyclones projected by large-ensemble simulations. J. Meteor. Soc. Japan. Ser. II 97. https://doi.org/10.2151/jmsj.2019-007.

Kusunoki, S., Mizuta, R., 2008. Future changes in the Baiu rain band projected by a 20 km mesh global atmospheric model: sea surface temperature dependence. SOLA 4, 85–88. https://doi.org/10.2151/sola.2008-022.

Kusunoki, S., Mizuta, R., Matsueda, M., 2011. Future changes in the East Asian rain band projected by global atmospheric models with 20 and 60 km grid size. Clim. Dynam. 37, 2481–2493. https://doi.org/10.1007/s00382-011-1000-x.

Kusunoki, S., Arakawa, O., 2015. Are CMIP5 models better than CMIP3 models in simulating precipitation over East Asia? J. Clim. 28 (14), 5601–5621.

Kusunoki, S., 2016. Is the global atmospheric model MRI-AGCM3. 2 better than the CMIP5 atmospheric models in simulating precipitation over East Asia? Clim. Dynam. 1–22. https://doi.org/10.1007/s00382-016-3335-9.

Li, W., Li, L., Ting, M., Liu, Y., 2012. Intensification of Northern Hemisphere subtropical highs in a warming climate. Nat. Geosci. 5 (11), 830–834.

Lin, J.-L., 2007. The double-ITCZ problem in IPCC AR4 Coupled GCMs: ocean-atmosphere feedback analysis. J. Clim. 20 (18), 4497–4525. https://doi.org/10.1175/JCLI4272.1.

Li, G., Xie, S.-P., 2014. Tropical biases in CMIP5 multimodel ensemble: the excessive equatorial Pacific cold tongue and double ITCZ problems. J. Clim. 27 (4), 1765–1780. https://doi.org/10.1175/JCLI-D-13-00337.1.

Ma, J., Xie, S.P., 2013. Regional patterns of sea surface temperature change: a source of uncertainty in future projections of precipitation and atmospheric circulation. J. Clim. 26 (8), 2482–2501.

Meehl, G.A., Boer, G.J., Covey, C., Latif, M., Stouffer, R.J., 2000. The coupled model intercomparison project (CMIP). Bull. Am. Meteorol. Soc. 81 (2), 313–318.
Meehl, G.A., Covey, C., Delworth, T., Latif, M., McAvaney, B., Mitchell, J.F., et al., 2007. The WCRP CMIP3 multimodel dataset: a new era in climate change research. Bull. Am. Meteorol. Soc. 88 (9), 1383–1394.
Meinshausen, M., Smith, S.J., Calvin, K., Daniel, J.S., Kainuma, M.L., Lamarque, J.F., et al., 2011. The RCP greenhouse gas concentrations and their extensions from 1765 to 2300. Climatic Change 109 (1), 213–241.
Mizuta, R., Yoshimura, H., Murakami, H., Matsueda, M., Endo, H., Ose, T., et al., 2012. Climate simulations using MRI-AGCM3. 2 with 20-km grid. J. Meteorol. Soc. Jpn. Ser. II 90, 233–258.
Mizuta, R., Arakawa, O., Ose, T., Kusunoki, S., Endo, H., Kitoh, A., 2014. Classification of CMIP5 future climate responses by the tropical sea surface temperature changes. Solanus 10, 167–171.
co-authors Mizuta, R., 2017. Over 5000 years of ensemble future climate simulations by 60km global and 20km regional atmospheric models. Bull. Am. Meteorol. Soc.. https://doi.org/10.1175/BAMS-D-16-0099.1.
Park, J., Kim, H., Wang, S.Y.S., Jeong, J.H., Lim, K.S., LaPlante, M., Yoon, J.H., 2020. Intensification of the East Asian summer monsoon lifecycle based on observation and CMIP6. Environ. Res. Lett. 15 (9), 0940b9.
Rayner, N.A.A., Parker, D.E., Horton, E.B., Folland, C.K., Alexander, L.V., Rowell, D.P., et al., 2003. Global analyses of sea surface temperature, sea ice, and night marine air temperature since the late nineteenth century. J. Geophys. Res. Atmos. 108 (D14).
Sillmann, J., Kharin, V.V., Zhang, X., Zwiers, F.W., Bronaugh, D., 2013. Climate extremes indices in the CMIP5 multimodel ensemble: Part 1. Model evaluation in the present climate. J. Geophys. Res. Atmos. 118 (4), 1716–1733.
Shaw, T.A., Voigt, A., 2015. Tug of war on summertime circulation between radiative forcing and sea surface warming. Nat. Geosci. 8 (7), 560–566.
Song, F., Leung, L.R., Lu, J., Dong, L., 2018. Seasonally dependent responses of subtropical highs and tropical rainfall to anthropogenic warming. Nat. Clim. Change 8 (9), 787–792.
Sugi, M., Kawamura, R., Sato, N., 1997. A study of SST-forced variability and potential predictability of seasonal mean fields using the JMA global model. J. Meteorol. Soc. Jpn. Ser. II 75 (3), 717–736.
Taylor, K.E., Stouffer, R.J., Meehl, G.A., 2012. An overview of CMIP5 and the experiment design. Bull. Am. Meteorol. Soc. 93 (4), 485–498.
Wang, B., Lin, H., 2002. Rainy season of the Asian–Pacific summer monsoon. J. Clim. 15 (4), 386–398.
Wang, S.S.Y., Kim, H., Coumou, D., Yoon, J.H., Zhao, L., Gillies, R.R., 2019. Consecutive extreme flooding and heat wave in Japan: are they becoming a norm? Atmos. Sci. Lett. 20 (10), e933.
Wilks, D.S., 2011. In: Statistical Methods in the Atmospheric Sciences, third ed. Academic press (Chapter 5) Frequentist Statistical Inference.
Xie, S.P., Deser, C., Vecchi, G.A., Collins, M., Delworth, T.L., Hall, A., et al., 2015. Towards predictive understanding of regional climate change. Nat. Clim. Change 5 (10), 921–930.
Ziese, M., Rauthe-Schöch, A., Becker, A., Finger, P., Rustemeier, E., Schneider, U., 2020. GPCC full data daily version 2020 at 1.0°: daily land-surface precipitation from rain-Gauges built on GTS-based and historic data. https://doi.org/10.5676/DWD_GPCC/FD_D_V2020_100.
Zhao, M., Held, I.M., Lin, S.J., Vecchi, G.A., 2009. Simulations of global hurricane climatology, interannual variability, and response to global warming using a 50-km resolution GCM. J. Clim. 22 (24), 6653–6678.